Assessment of ion kinetic effects in shock-driven inertial confinement fusion implosions using fusion burn imaging

M. J. Rosenberg, F. H. Séguin, P. A. Amendt, S. Atzeni, H. G. Rinderknecht, N. M. Hoffman, A. B. Zylstra, C. K. Li, H. Sio, M. Gatu Johnson, J. A. Frenje, R. D. Petrasso, V. Yu. Glebov, C. Stoeckl, W. Seka, F. J. Marshall, J. A. Delettrez, T. C. Sangster, R. Betti, S. C. Wilks, J. Pino, G. Kagan, K. Molvig, and A. Nikroo

Citation: Physics of Plasmas (1994-present) **22**, 062702 (2015); doi: 10.1063/1.4921935
View online: http://dx.doi.org/10.1063/1.4921935
View Table of Contents: http://scitation.aip.org/content/aip/journal/pop/22/6?ver=pdfcov
Published by the AIP Publishing

Assessment of ion kinetic effects in shock-driven inertial confinement fusion implosions using fusion burn imaging

M. J. Rosenberg,[1,a)] F. H. Séguin,[1] P. A. Amendt,[2] S. Atzeni,[3] H. G. Rinderknecht,[1] N. M. Hoffman,[4] A. B. Zylstra,[1] C. K. Li,[1] H. Sio,[1] M. Gatu Johnson,[1] J. A. Frenje,[1] R. D. Petrasso,[1] V. Yu. Glebov,[5] C. Stoeckl,[5] W. Seka,[5] F. J. Marshall,[5] J. A. Delettrez,[5] T. C. Sangster,[5] R. Betti,[5] S. C. Wilks,[2] J. Pino,[2] G. Kagan,[4] K. Molvig,[4] and A. Nikroo[6]
[1]*Plasma Science and Fusion Center, Massachusetts Institute of Technology, Cambridge, Massachusetts 02139, USA*
[2]*Lawrence Livermore National Laboratory, Livermore, California 94550, USA*
[3]*Dipartimento SBAI, Università di Roma "La Sapienza" and CNISM, Via A. Scarpa 14-16, I-00161 Roma, Italy*
[4]*Los Alamos National Laboratory, Los Alamos, New Mexico 87545, USA*
[5]*Laboratory for Laser Energetics, University of Rochester, Rochester, New York 14623, USA*
[6]*General Atomics, San Diego, California 92186, USA*

(Received 15 February 2015; accepted 15 May 2015; published online 2 June 2015)

The significance and nature of ion kinetic effects in D^3He-filled, shock-driven inertial confinement fusion implosions are assessed through measurements of fusion burn profiles. Over this series of experiments, the ratio of ion-ion mean free path to minimum shell radius (the Knudsen number, N_K) was varied from 0.3 to 9 in order to probe hydrodynamic-like to strongly kinetic plasma conditions; as the Knudsen number increased, hydrodynamic models increasingly failed to match measured yields, while an empirically-tuned, first-step model of ion kinetic effects better captured the observed yield trends [Rosenberg *et al.*, Phys. Rev. Lett. **112**, 185001 (2014)]. Here, spatially resolved measurements of the fusion burn are used to examine kinetic ion transport effects in greater detail, adding an additional dimension of understanding that goes beyond zero-dimensional integrated quantities to one-dimensional profiles. In agreement with the previous findings, a comparison of measured and simulated burn profiles shows that models including ion transport effects are able to better match the experimental results. In implosions characterized by large Knudsen numbers ($N_K \sim 3$), the fusion burn profiles predicted by hydrodynamics simulations that exclude ion mean free path effects are peaked far from the origin, in stark disagreement with the experimentally observed profiles, which are centrally peaked. In contrast, a hydrodynamics simulation that includes a model of ion diffusion is able to qualitatively match the measured profile shapes. Therefore, ion diffusion or diffusion-like processes are identified as a plausible explanation of the observed trends, though further refinement of the models is needed for a more complete and quantitative understanding of ion kinetic effects. © *2015 AIP Publishing LLC*.
[http://dx.doi.org/10.1063/1.4921935]

I. INTRODUCTION

The converging shock phase of hot-spot inertial confinement fusion (ICF) implosions[1] is characterized by high temperatures ($T_i > 5\,\mathrm{keV}$) and moderate densities ($n_i \sim 10^{22}\,\mathrm{cm}^{-3}$), so that the ion—ion mean free path becomes long relative to relevant length scales, such as the radius of the converging shock or shell. Under these conditions, a hydrodynamic description of the plasma as a Maxwellian fluid with relatively gentle gradients becomes invalid and ion kinetic effects become significant.

Shock-driven exploding-pusher implosions[2–5] are an ideal platform to isolate and probe ion kinetic and multiple-ion-fluid effects in ICF implosions,[6,7] as the bulk of fusion reactions (and diagnosis of implosion conditions) occurs when the plasma is at kinetic-like conditions. Previous experimental and theoretical work has explored deviations from hydrodynamic behavior in ICF implosions. Yield anomalies observed in mixed-fuel implosions such as D^3He,[8] DT,[9] and DT^3He (Ref. 10) have been partially explained by multiple-ion models that include barodiffusion, electrodiffusion, and thermodiffusion.[11–14] Models allowing for Knudsen-layer losses of suprathermal ions and a deviation from Maxwellian ion distributions[15,16] have produced better agreement with the results of shock-driven implosions, and kinetic simulations have been found to predict weaker shock-front gradients and shock-induced fusion yields than in hydrodynamic simulations,[17,18] in better agreement with experimental results. Shock-driven implosion experiments have also demonstrated enhanced diffusion of fuel and shell ions and multiple-ion effects under kinetic-like conditions.[7,19]

Recently, a series of shock-driven implosions showed the breakdown of hydrodynamic models and the impact of ion kinetic effects on implosion performance for large ion-ion mean free path (λ_{ii}) or Knudsen number ($N_K \equiv \lambda_{ii}/R_{shell}$,

[a)]Present address: Laboratory for Laser Energetics, University of Rochester. Electronic mail: mros@lle.rochester.edu.

the ratio of ion-ion mean free path to the minimum shell radius).[6] These experiments effectively spanned the regimes of hydrodynamic-like ($N_K < 1$) to strongly kinetic ($N_K > 1$) plasma conditions. The trend of measured yields relative to hydrodynamically simulated yields with respect to Knudsen number in these experiments on the OMEGA laser facility,[20] as well as in other exploding pusher experiments at the National Ignition Facility (NIF),[21] previously shown in Ref. 22, is presented for background in Figure 1. Overall, these different experiments illustrate how ion kinetic effects start to become significant in implosions with $N_K \gtrsim 0.1$. Over the range of the OMEGA experiments ($0.3 \lesssim N_K \lesssim 9$), the ratio of measured DD fusion yields (see Eq. (1)) to the yields predicted by radiation-hydrodynamics simulations is a strongly decreasing function of the Knudsen number. These results signify the increasing impact of ion kinetic effects on implosion performance with longer ion mean free paths.

To investigate in greater depth the ion kinetic physics that becomes significant at high N_K, this work presents measurements of spatially resolved fusion burn profiles in these OMEGA shock-driven implosion experiments. The measured burn profiles are compared to the predictions of purely hydrodynamic models and hydrodynamic models that have been modified to account for some ion transport effects. As these long-mean-free-path effects are the result of kinetic spatial transport mechanisms for either thermal or suprathermal ions, spatially resolved measurements are able to more directly assess the nature and magnitude of these kinetic processes. It is shown that for hydrodynamic-like fuel conditions, purely hydrodynamic models reasonably capture the burn profile shape, but for strongly kinetic fuel conditions,

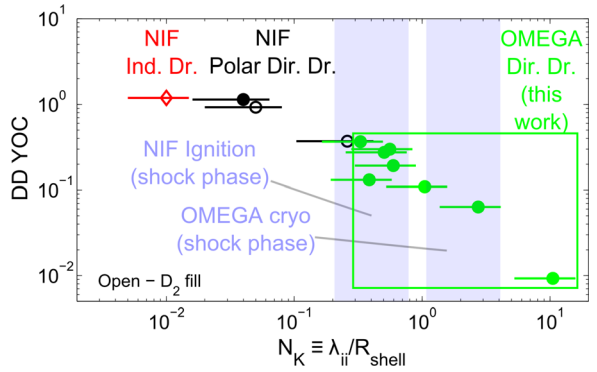

FIG. 1. Ratio of measured DD fusion yields to hydrodynamics-simulated yields (yield over clean, YOC) as a function of the Knudsen number (N_K) for an indirect-drive exploding pusher on NIF (red diamond),[23] three polar-direct-drive (PDD)[24] exploding pushers on NIF,[22] and direct-drive exploding pushers on OMEGA (green circles).[6] Fusion burn profile measurements of the OMEGA experiments are described herein. Filled markers represent D^3He-filled implosions, while open markers denote D_2-filled implosions. Though the drive conditions are quite different, these experiments show a unified picture of the increasing impact of ion kinetic effects as a function of increasing Knudsen number for $N_K \gtrsim 0.1$. A band centered around $N_K = 0.5$ shows the approximate Knudsen number at the center of a NIF ignition-relevant indirect-drive implosion[25] or a NIF polar-direct-drive implosion[24] immediately after shock convergence, while a band centered around $N_K = 2$ shows the approximate Knudsen number after shock convergence at the center of a cryogenic layered implosion on OMEGA.[26] This data were originally presented in Ref. 22. Reproduced with permission from Phys. Plasmas **21**, 122712 (2014).

hydrodynamics-generated burn profiles qualitatively agree with measurements only with a modification of ion transport effects, such as the inclusion of ion diffusion. Though further refinement of the models is required to produce better quantitative agreement with the data, these results provide additional and more specific evidence, in support of previous findings, on the importance of kinetic ion transport processes under long mean-free-path conditions, which are prevalent during the shock convergence phase of ICF implosions.

This paper is organized as follows: the experimental setup, including capsule and laser parameters, and the spatial burn profile measurement technique are discussed in Sec. II; the mainline and ion-transport-modified hydrodynamics models used to simulate the implosions are described in Sec. III; experimental burn profile data are presented in Sec. IV; the physics implications of the results inferred through a comparison to various models, as well as future work, are discussed in Sec. V; and concluding remarks are presented in Sec. VI.

II. EXPERIMENTS

As has been described previously,[6] a series of thin-glass-shell implosions were performed on the OMEGA laser facility[20] to study ion kinetic effects. The SiO_2 capsules had an outer diameter of $860 \pm 12\,\mu$m and a wall thickness of $2.3 \pm 0.1\,\mu$m and were filled with a variety of fill densities of equimolar D^3He gas, ranging from 0.14 to 3.1 mg/cm^3. The capsules were imploded by 59 or 60 nominally symmetrically pointed beams, delivering 14.6 kJ in a 0.6-ns pulse. In these experiments, rapid laser absorption in the thin SiO_2 ablator causes a strong, spherically converging shock to be launched into the gas with a resulting Mach number of $M \sim 15$. After the shock rebounds at the origin, DD and D^3He fusion reactions occur along and behind the rebounding shock trajectory. For decreasing initial gas density, the Maxwellian-average mean free path for ion-ion collisions around nuclear bang time varied from $\sim 40\,\mu$m, in a regime that may be more reasonably described by hydrodynamics ($N_K \sim 0.3$), to $\sim 800\,\mu$m, in a regime that is strongly kinetic ($N_K \sim 9$).

Nuclear diagnostics, including the use of fusion burn imaging, were used to determine implosion conditions and, through comparison to model predictions, assess the impact of ion mean free path effects. The fusion burn profile measurements utilized both protons from DD reactions

$$\mathrm{D} + \mathrm{D} \rightarrow \mathrm{T}(1.01\,\mathrm{MeV}) + \mathrm{p}(3.02\,\mathrm{MeV}), \tag{1}$$

and protons from D^3He reactions

$$\mathrm{D} + {}^3\mathrm{He} \rightarrow \alpha(3.6\,\mathrm{MeV}) + \mathrm{p}(14.7\,\mathrm{MeV}). \tag{2}$$

The experimental setup for fusion burn profile measurements using the penumbral imaging technique of the Proton Core Imaging System (PCIS)[27–29] is shown in Figure 2. Two pieces of CR-39 were used to detect protons: the front piece, filtered by 5 μm Ta and 12.5 μm Al, was used to detect DD protons; the second piece, additionally filtered by $\sim 1100\,\mu$m of CR-39 (the first piece) and 400 μm Al, was used to detect

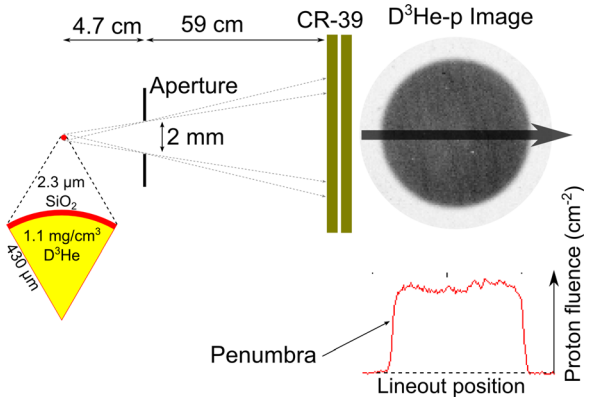

FIG. 2. Experimental setup for penumbral fusion burn imaging using the Proton Core Imaging System (PCIS), for an implosion with 1.1 mg/cm^3 D^{3}He. DD-p and D^{3}He-p are detected on separate pieces of CR-39, though only a D^{3}He-p image is shown. The penumbra are analyzed to infer profiles of proton emission. While in this diagram a horizontal lineout is depicted, in analysis the penumbra is azimuthally averaged around the image and is much smoother than what is shown here.

D^{3}He protons.[30] Raw proton fluence images, an example of which is shown on the right side of Figure 2, are analyzed to infer time-integrated profiles of fusion emission.

The penumbral images can be used to study the two dimensional surface brightness of proton emission in the implosion (Ref. 27 and other work to be published). Here another approach is taken,[27,29] assuming that the implosion is spherically symmetric and studying the burn-averaged, radial profile of reactions per unit volume, $S(r)$, in the implosion. A three-parameter family of source functions is used, as described in Appendix A. As shown in Figure 3, the shape of the profile is defined by a single "peakedness" parameter p, which is positive for centrally peaked profiles, equal to 0 for flat profiles, and negative for hollow profiles. The size of the burn region is defined by a parameter R_{50}, which is the median burn radius (containing 50% of the total reaction yield). The total burn-averaged yield depends on a multiplier S_0. This 1D simplification is a reasonable assumption for the symmetrically illuminated shock-driven implosions of interest here, which are not generally susceptible to 2D and 3D hydrodynamic effects.[7]

It will be shown below that the measured burn profiles exhibit centrally peaked behavior, in contrast to mainline hydrodynamic models (excluding ion diffusive effects) of implosions with low initial gas density and long ion mean free paths, which predict hollow burn profiles.

III. MODELS

Several different models have been used to understand burn profile measurements and to infer the significance of ion kinetic effects, including purely hydrodynamic models as well as models that attempt to account for ion transport effects such as diffusion.

Radiation-hydrodynamics simulations were performed using the 1D Lagrangian code DUED,[32,33] which includes flux-limited electron thermal transport with a flux limiter of $f = 0.07$, multigroup radiative diffusion, and non-LTE opacities. Laser absorption is modeled by inverse bremsstrahlung, with laser refraction such that the simulated absorbed laser fraction matches measurements by full aperture backscatter stations (FABS).[34] An ion viscosity model is included, which mitigates a (non-physical) temperature spike at the origin at shock convergence in a 1D model. The ion viscosity flux limiter (vfl) is varied in different simulations, but is typically set at vfl = 1. The model also accounts for ion thermal conduction. As an example, the DUED simulation of an implosion with 1.1 mg/cm^3 D^{3}He is shown in Figure 4. Lagrangian mass-element trajectories as a function of time (Figure 4(a)) show a rapidly converging shock, which rebounds at the center of the implosion. The burn occurs near the end of the laser pulse (Figure 4(b)), with the timing of the DD-n reaction history as measured by the neutron temporal diagnostic (NTD)[35] in fairly good agreement with the DUED prediction. For comparison to PCIS data, simulated spatial burn profiles are time-integrated over the duration of the reaction history.

Radiation-hydrodynamics simulations were also performed using the 1D LASNEX code,[36] including inverse bremsstrahlung absorption, multigroup radiative diffusion, and flux-limited electron thermal transport with a flux limiter of 0.071. As in DUED, physical ion viscosity was used. To account for ion transport effects that are expected to be significant in these implosions, some LASNEX simulations were also run with a model of classical ion diffusion included,[37] which models diffusion of D, ^{3}He, Si, and O ions across the D^{3}He fuel/SiO$_2$ shell interface. The comparison of experimental burn profiles with LASNEX simulations excluding and including ion diffusion, which provides strong evidence of the significance of ion transport effects, will be discussed in Sec. V.

Additional radiation-hydrodynamics simulations were performed using the 1D HYADES code,[38] which includes multigroup radiative diffusion, flux-limited electron thermal

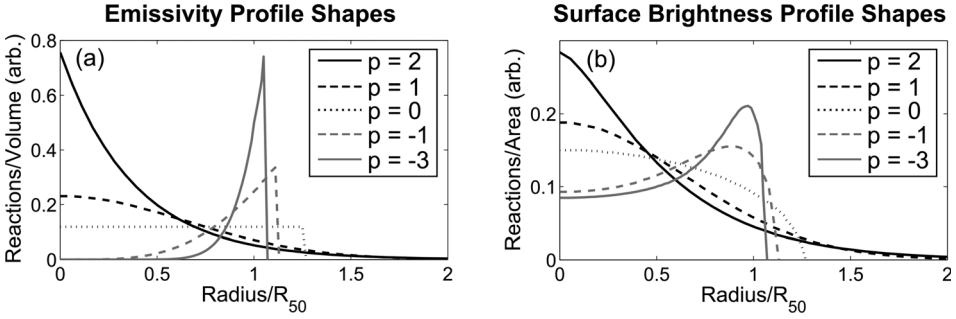

FIG. 3. Family of curves for (a) local fusion emissivity, based on different values of the peakedness parameter p, for analysis of PCIS data.[31] While emissivity is the preferred and more physically intuitive quantity and is more directly calculated in the PCIS analysis, some simulations give instead surface brightness (the line-of-sight integral of the radial emissivity profile) for comparison to the experimental data. The corresponding family of surface brightness profiles is illustrated in (b).

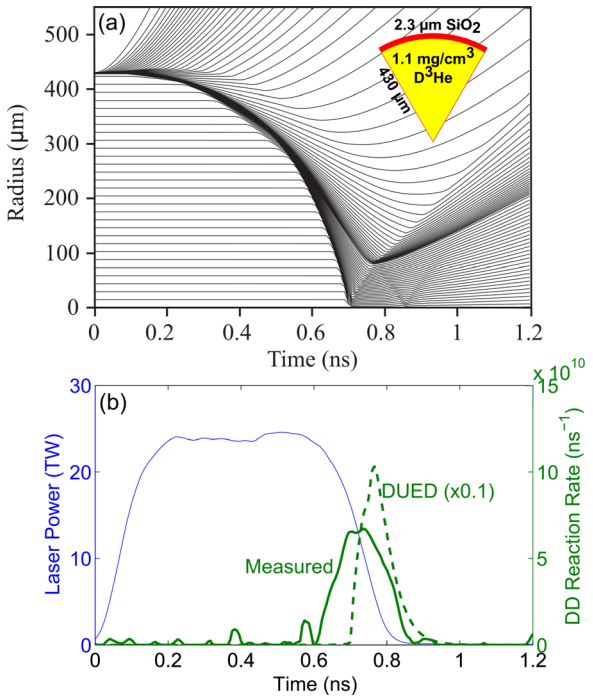

FIG. 4. (a) Lagrangian mass-element trajectories and DD fusion reaction rate per unit volume in 1D DUED simulations of an implosion with 1.1 mg/cm^3 D^{3}He, originally presented in Ref. 6. (b) The DUED-predicted DD burn history (green dashed) compared to the measured burn history (green solid) and the incident laser power (blue solid). (a) is reproduced with permission from Phys. Rev. Lett. **112**, 185001 (2014).

transport with a flux limiter of $f = 0.07$, and inverse bremsstrahlung laser absorption, with the total absorption fraction set by the full aperture backcsatter stations (FABS)[34] measurements of 0.58 on these experiments. Though these HYADES simulations did not include either ion viscosity or ion diffusion, they serve as a useful benchmark for comparison to other hydrodynamic models and to the experimental data.

A first step implementation of ion kinetic effects into a mainline ICF code, the reduced ion-kinetic (RIK) model[39] has also generated predicted burn profile results for comparison to experimental data. This simulation technique incorporates reduced models of ion kinetic effects in a 1D fluid-based radiation-hydrodynamic code, to represent the effects of kinetic transport of ion mass, momentum, and thermal energy, and reduction in fusion reactivity owing to modified ion-distribution tails when $\lambda_{ii} \sim R_{shell}$.[16,40,41] As was described in Ref. 6, model parameters were constrained by the measured DD and D^{3}He yields, DD-burn-averaged T_i, DD bang time, and the laser absorption fraction. The code uses multigroup radiation diffusion, flux-limited electron thermal diffusion ($f = 0.06$), and laser energy propagation via geometric ray tracing and deposition by inverse bremsstrahlung, with laser deposition inferred from the observed bang time and absorption fraction.

By comparing the measured fusion burn profiles to the predicted burn profiles of pure hydrodynamic models and hydrodynamic models that include ion transport effects, evidence of the impact and magnitude of kinetic or ion mean free path effects is inferred. The impact of different modeling options on the simulated results is summarized in Table I and is illustrated and discussed in more detail in Sec. V and Appendix B.

IV. RESULTS

Spatially resolved measurements of DD-p and D^{3}He-p emission have been obtained over the range of initial gas densities. Radial burn profiles for both DD and D^{3}He reactions, at an initial gas density of 3.1 mg/cm^3, in the hydrodynamic-like regime ($N_K \sim 0.3$), and at an initial gas density of 0.4 mg/cm^3, in the kinetic regime ($N_K \sim 3$), are shown in Figure 5. These profiles are inferred by a forward fit to measurements of the radial derivative of proton fluence in the PCIS images, which are shown in Appendix A. Across the range of initial gas densities sampled in these experiments, including the examples shown in Figure 5, both fusion-product measurements show centrally peaked burn profiles. The shape parameter varied only slightly, and fell within the sub-Gaussian range for all implosions: $p_{DD} = 1.54 \pm 0.98$ and $p_{D3He} = 1.48 \pm 0.28$ at 0.4 mg/cm^3, while $p_{DD} = 1.93 \pm 0.87$ and $p_{D3He} = 1.61 \pm 0.49$ at 3.1 mg/cm^3. Though the shape uncertainty is somewhat large, the allowed solutions all fall within the range of centrally peaked profiles ($p > 1$). Later, it will be shown that for low-initial-gas-density implosions, hydrodynamic models without ion diffusion or flux-limited ion viscosity predict burn

TABLE I. Modeling options, specifically the treatment of ion viscosity and ion diffusion—and their impact—in LASNEX, DUED, HYADES, and RIK simulations. When physical ion viscosity is implemented, the value of the viscosity flux limiter (vfl) is specified.

	Ion viscosity		Ion diffusion	
Code	Treatment	Effect	Treatment	Effect
LASNEX	Artificial and physical (vfl = 1)	Hollow profiles at low initial gas density	Classical[37]	Recovers centrally peaked profiles, reduces yield (too much) in low-density implosions
DUED	Artificial and physical (vfl = 1 but is varied)	Hollow profiles for vfl = 1, centrally peaked for lower vfl; yield unaffected	None	—
HYADES	Artificial only	Flat profiles at low density, sharply peaked profiles at high density	None	—
RIK	Artificial only	Anecdotally, inclusion of physical ion viscosity has minimal impact on yield	Classical[37] Knudsen layer[40]	Recovers experimental yields, but burn radii too small

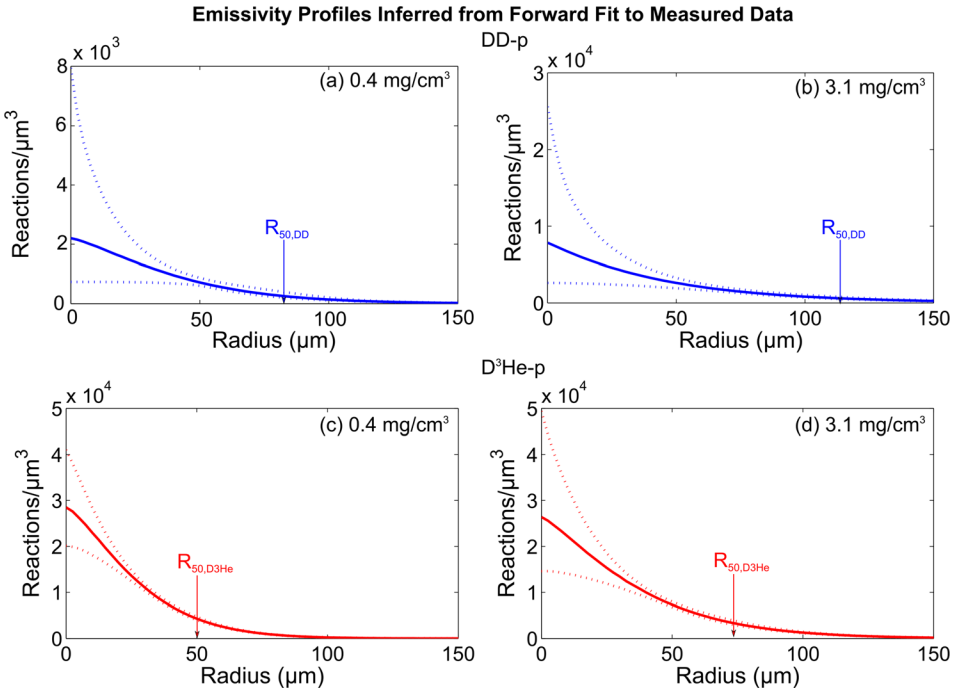

FIG. 5. Measured profiles of fusion emissivity for (a)-(b) DD-p (blue) and (c)-(d) D^3He-p (red) in shock-driven implosions filled with (a),(c) 0.4 mg/cm^3 D^3He gas, in the kinetic regime, and (b),(d) 3.1 mg/cm^3 D^3He gas, in the hydrodynamic-like regime. The solid lines represent the best fit, while the dotted lines represent uncertainty bounds. Burn profiles are centrally peaked for both reactions at both low and high initial gas density. The radii containing 50% of fusion reactions, R_{50}, are indicated.

profiles of a qualitatively different shape, in stark disagreement with the measurements.

The measured burn profile size is well constrained, with $R_{50,DD} = 77.3 \pm 8.1\ \mu$m and $R_{50,D3He} = 50.0 \pm 1.9\ \mu$m at 0.4 mg/cm^3 and $R_{50,DD} = 113.6 \pm 13.0\ \mu$m and $R_{50,D3He} = 74.4 \pm 3.8\ \mu$m at 3.1 mg/cm^3. The measured DD-p and D^3He-p burn profile sizes (R_{50}) as a function of initial gas density are summarized in Figure 6. Both reactions show a trend of increasing burn radius with increasing gas density. This trend possibly reflects a weak trend of decreasing shell convergence with increasing gas density—as reactions occur along and behind the rebound trajectory of the shock before it runs into the shell—and likely also a trend of stronger ion kinetic effects (e.g., ion diffusion and Knudsen layer effects) preferentially reducing burn near the fuel-shell interface at lower initial gas densities. Additionally, the data in Figure 6 show a fairly persistent differential between the DD and D^3He burn radii, widening slightly from $\Delta R_{50} \equiv R_{50,DD} - R_{50,D^3He} = 20.5 \pm 8.3\ \mu$m at 0.14 mg/cm^3 to $\Delta R_{50} = 39.2 \pm 13.5\ \mu$m at 3.1 mg/cm^3. This differential in the higher-density implosions

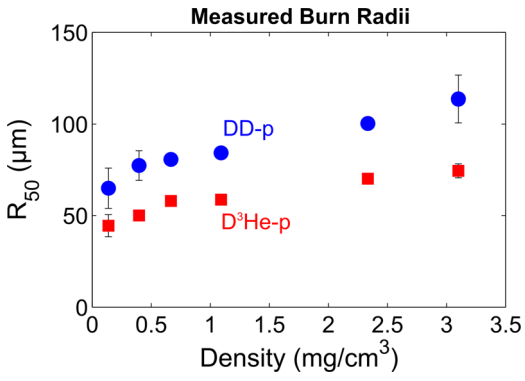

FIG. 6. Measured DD-p (blue circles) and D^3He-p (red squares) burn radii (characterized in terms of R_{50}) as a function of initial gas density.

is likely indicative of ion temperature gradients, which give rise to differences between D^3He and DD reaction profiles due to the different temperature sensitivities of the two reactions (D^3He being more strongly weighted by the hotter regions of the fuel). In lower-density implosions, for which purely hydrodynamic codes predict $\Delta R_{50} \sim 0$, the persistence of a differential between burn radii could be a signature of ion diffusion or other kinetic ion transport effects, which are expected to be quite significant in this $N_K > 1$ plasma and which allow for deuterium ions to be transported farther from the center of the implosion than ^3He ions. These ion species separation effects[19] may also contribute to ΔR_{50} in the higher-density implosions.

V. DISCUSSION: COMPARISON TO SIMULATIONS

To assess the impact of ion mean free path effects, measured burn profile results have been compared to the predictions of hydrodynamic simulations excluding and including some of the effects that are likely to be significant, in particular ion diffusion.

The comparison of measured burn profile data to LASNEX simulations illustrates the significance of ion diffusion (or physical processes similar to diffusion) under long-λ_{ii}, high-N_K conditions. Figure 7 shows measured profiles of the surface brightness of proton emission in comparison to profiles of surface brightness predicted by pure-hydro LASNEX simulations and by LASNEX simulations that include classical ion diffusion.[37] As was shown in Figure 5, the measured emission profiles are centrally-peaked over the entire range of initial gas densities. In contrast, the purely hydrodynamic LASNEX simulations show centrally peaked surface brightness profiles only at high initial gas densities (3.1 mg/cm^3); at low initial gas densities (0.4 mg/cm^3) the surface brightness profile is peaked far from the center, with most of the fusion reactions occurring in a thin region of burn close to the fuel-

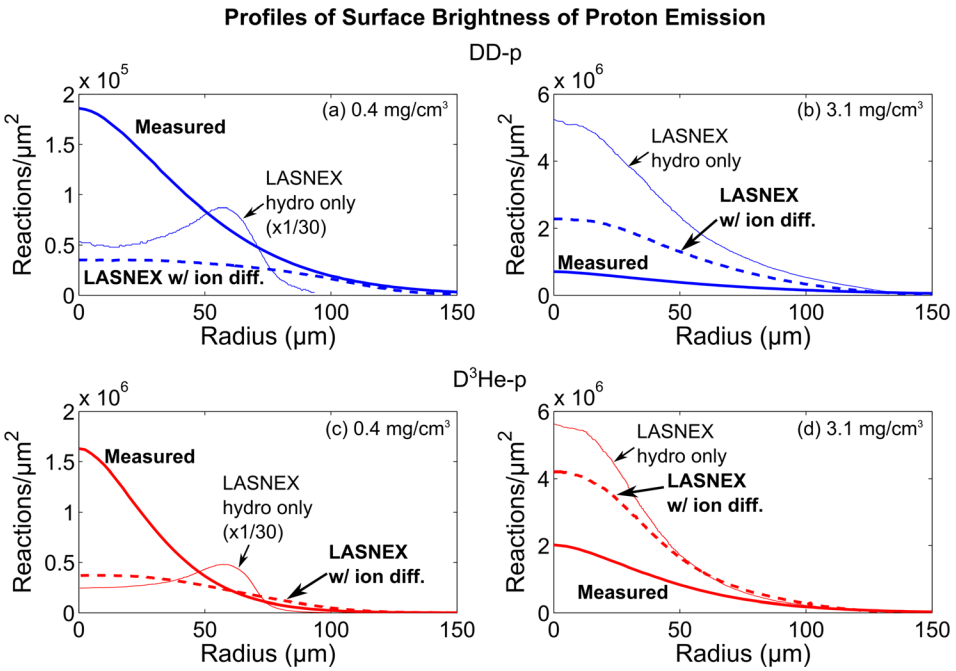

FIG. 7. Profiles of surface brightness of (a)-(b) DD-proton (blue) and (c)-(d) D^3He-proton (red) emission in LASNEX simulations and the measured data (thick solid lines), for implosions with initial gas densities of 0.4 mg/cm^3 (left) and 3.1 mg/cm^3 (right). LASNEX simulations have been performed either with pure hydrodynamics (thin solid lines) or with ion diffusion included (thick dashed lines). In (a) and (c) the hydro only LASNEX values have been reduced by a factor of 30 so that they appear on the same scale as the other curves. The measured surface brightness profiles correspond to the emissivity profiles shown in Figure 5. At low initial gas density (long ion mean free path, $N_K \sim 3$), ion diffusion is able to capture the shape of the measured surface brightness profile.

shell interface. The shape of the hydro-only LASNEX profiles at 0.4 mg/cm^3 is most similar to the $p = -1$ or $p = -3$ curves shown in Figure 3(b). This value is strongly inconsistent with the measured $p \sim 1.5$ at 0.4 mg/cm^3. In this low-density, $N_K \sim 3$ case, the inclusion of ion diffusion in LASNEX causes a significant change in the simulated surface brightness profile shape, producing a centrally peaked profile qualitatively similar to what is observed experimentally. In this case, ion diffusion across the fuel-shell interface also drastically reduces (by a factor of ~30) the overall predicted yields, and preferentially reduces the number of reactions near the shell. The D and ^{3}He ions, which have mean free paths in the D^3He fuel of 460 μm and 140 μm, respectively, readily escape the fuel region (of radius 90 μm) and penetrate into the shell, where fusion reactions are largely suppressed. The fuel ions have mean free paths in the SiO_2 shell of order 10–20 μm, indicating that they traverse a fair distance beyond the fuel-shell interface. In the high-density, $N_K \sim 0.3$ case, ion diffusion has only a modest impact on the reaction profiles: the surface brightness profile shapes are only minimally altered, and the magnitude of the profiles does not change significantly. This result too makes sense, based on ion mean free paths within the fuel of only 80 μm for D and 25 μm for ^{3}He (compared to the fuel radius of 130 μm), and

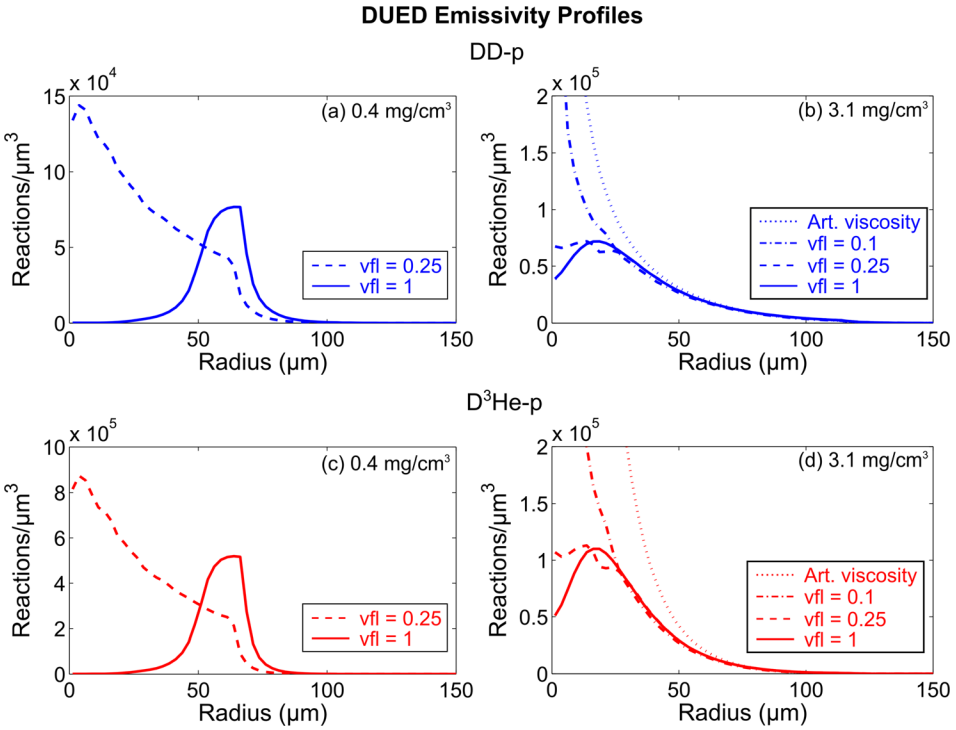

FIG. 8. DUED-simulated fusion emission profiles of (a)-(b) DD-p (blue) and (c)-(d) D^3He-p (red), for implosions with initial gas densities of 0.4 mg/cm^3 (left) and 3.1 mg/cm^3 (right). These profiles can be directly compared to the measured emissivity profiles shown in Figure 5. The modeling of ion viscosity was varied, from only artificial viscosity to models that include also physical ion viscosity with different values of the viscosity flux limiter (vfl). A viscosity flux limiter of 0.25 produces the best agreement with the experimental data.

ion mean free path of fuel ions within the shell of only 5–10 μm.

DUED-simulated profiles of fusion emission for both DD-p and D^3He-p provide additional evidence of how ion transport effects, in this case manifest as a reduction of ion viscosity, can plausibly explain the experimentally measured burn profile shapes. DD-p and D^3He-p emission profiles predicted by DUED, using different implementations of ion viscosity, are shown in Figure 8 for experiments at 0.4 mg/cm^3 and 3.1 mg/cm^3 initial gas density. Artificial (Schulz) viscosity[42] is used in all simulations, and in most simulations, real ion viscosity is included as well, with different values of the ion viscosity flux limiters (vfl) in different simulations. At 3.1 mg/cm^3, the simulations with only artificial viscosity show very sharply peaked profiles. The inclusion of ion viscosity reduces the number of reactions near the center of the implosion, so that with full ion viscosity (vfl = 1) the profiles are no longer centrally peaked. At 0.4 mg/cm^3, a similar trend is observed, where a viscosity flux limiter of vfl = 1 produces reaction profiles peaked far from the center, similar to what is predicted by LASNEX without ion diffusion (Figure 7(a)). A viscosity flux limiter of vfl = 0.25 instead produces profiles in DUED that are centrally peaked. In comparison to the measured profiles (Figure 5), which are centrally peaked, it appears that a lowering of the viscosity flux limiter is needed, and that vfl = 1 exaggerates the actual effect of viscosity in the experiments. Thus, the reduction of ion viscosity flux limiter in DUED has a similar effect on the burn profile shapes as the inclusion of ion diffusion in LASNEX. (Notably, it is observed in LASNEX simulations without ion diffusion that the reduction of ion viscosity flux limiter has a similar impact on the burn profile shapes as in DUED.) As discussed below, the impact of these modifications in LASNEX and DUED on other simulated observables is somewhat different, and this apparent inverse relationship between viscosity and diffusion as it relates to the burn profile shape is not yet understood and is currently under study. This DUED result is a further indication that under high-Knudsen-number conditions, the usual treatment of ion transport in mainline hydrodynamic codes is inadequate, suggesting that ion mean free path effects have a substantial impact.

Overall, these reaction profile results provide further evidence in support of what was observed previously with the experimental and simulated yields, where hydrodynamics codes are unable to capture key physics in high-N_K experiments, though they perform more adequately in low-N_K experiments, and that ion diffusion is likely largely responsible.[6] However, while the burn profiles results presented here corroborate that interpretation, quantitative differences between these simulations and the measured observables beyond the burn profile shape indicate that the modeling of ion kinetic effects needs further refinement. The remaining discrepancies are made evident by a comparison of measured yields to the yields predicted in the different simulations (Table II). The measured DD yields are obtained by neutron time of flight (nTOF)[43] measurements, while the D^3He yields are measured by wedge range filter (WRF) proton spectrometers.[44] The measured yields inferred from the PCIS burn profile data ($\int 4\pi r^2 S(r) dr$) are 30–50% lower than from nTOF and WRF,[45] so in this discussion PCIS is used only for the shape of the burn profiles, but nTOF and WRFs are used for the total yield.

In the 3.1 mg/cm^3 experiment, the inclusion of ion diffusion or the reduction of ion viscosity has only a small effect. The ratio of measured to pure-hydrodynamics LASNEX-simulated yields (the yield-over-simulated, YOS), was 0.54 for DD yield and 0.93 for D^3He yield, for an average YOS of 0.735. The inclusion of ion diffusion altered the average YOS only slightly, to 0.825, with $YOS_{DD} = 0.82$ and $YOS_{D3He} = 0.83$. LASNEX-simulated burn-averaged ion temperatures increased slightly with the inclusion of ion diffusion, from $T_{i,DD} = 9.5$ keV to $T_{i,DD} = 9.9$ keV (averaged over DD reactions) and from $T_{i,D3He} = 10.4$ keV to $T_{i,D3He} = 10.7$ keV (averaged over D^3He reactions), in comparison to the measured $T_{i,DD} = 12.2$ keV and $T_{i,D3He} = 14.5$ keV. The LASNEX-simulated burn radii likewise do not change significantly with the inclusion of ion diffusion, decreasing from $R_{50,DD} = 78$ μm to $R_{50,DD} = 73$ μm and $R_{50,D^3He} = 61$ μm to $R_{50,D^3He} = 56$ μm, in comparison to the measured $R_{50,DD} = 113.6$ μm and $R_{50,D3He} = 74.4$ μm. For DUED, the YOS with vfl = 1 was 0.37 for DD yield and 0.59 for D^3He yield. With vfl = 0.25 in DUED, the YOS was 0.38 for DD yield and 0.59 for D^3He yield. DUED-simulated burn-averaged ion temperatures and burn radii are also virtually unchanged with the reduction of ion viscosity, with $T_{i,DD} = 10.1$, $T_{i,D3He} = 11.9$ keV, $R_{50,DD} = 63$ μm and $R_{50,D3He} = 47$ μm for vfl = 1 and $T_{i,DD} = 10.1$, $T_{i,D3He} = 11.9$ keV, $R_{50,DD} = 62$ μm and $R_{50,D3He} = 47$ μm for vfl = 0.25. Even under these hydrodynamic-like conditions, the models are not able to perfectly capture the implosion conditions, though they appear to be qualitatively correct in total yield and the overall fusion emission profile.

In contrast, at 0.4 mg/cm^3, ion kinetic effects are likely to be more significant, and the treatment of ion transport effects has a larger impact in the simulations. Though this modeling

TABLE II. Measured and simulated DD and D^3He yields in implosions with 0.4 mg/cm^3 and 3.1 mg/cm^3 initial D^3He gas density. The simulations include purely hydrodynamics LASNEX (without ion diffusion), LASNEX with ion diffusion, DUED with an ion viscosity flux limiter of vfl = 1, and DUED with an ion viscosity flux limiter of vfl = 0.25.

Initial gas density (mg/cm^3)	Reaction	Measured yield	LASNEX yield		DUED yield	
			pure hydro	w/ion diff.	vfl = 1	vfl = 0.25
0.4	DD	5.48×10^9	3.9×10^{10}	1.1×10^9	9.1×10^{10}	8.2×10^{10}
	D^3He	2.33×10^{10}	1.9×10^{11}	6.4×10^9	5.0×10^{11}	4.1×10^{11}
3.1	DD	2.81×10^{10}	5.2×10^{10}	3.4×10^{10}	7.5×10^{10}	7.4×10^{10}
	D^3He	3.41×10^{10}	3.7×10^{10}	4.1×10^{10}	5.8×10^{10}	5.8×10^{10}

better reproduces the experimental results, the comparison of measured and simulated yields shows that the models implemented in LASNEX and DUED do not fully capture implosion conditions. Relative to hydrodynamics-only LASNEX simulations, $YOS_{DD} = 0.14$ and $YOS_{D3He} = 0.12$. The inclusion of ion diffusion alters those quantities to $YOS_{DD} = 4.98$ and $YOS_{D3He} = 3.64$. Concurrently, LASNEX-simulated burn-averaged ion temperatures decrease and burn radii increase, from $T_{i,DD} = 25.5\,\text{keV}$, $T_{i,D3He} = 27.3\,\text{keV}$, $R_{50,DD} = 68\,\mu\text{m}$, $R_{50,D3He} = 67\,\mu\text{m}$ to $T_{i,DD} = 23.6\,\text{keV}$, $T_{i,D3He} = 24.8\,\text{keV}$, $R_{50,DD} = 100\,\mu\text{m}$, $R_{50,D3He} = 80\,\mu\text{m}$, in comparison to the measured $T_{i,DD} = 19.3\,\text{keV}$, $T_{i,D3He} = 23.1\,\text{keV}$, $R_{50,DD} = 77.3\,\mu\text{m}$, $R_{50,D3He} = 50.0\,\mu\text{m}$. The reduction in yield and altering of the burn profile shape in LASNEX with the inclusion of ion diffusion is largely a consequence of modification of ion density profiles. In comparison to the measured results, the classical ion diffusion model in LASNEX overestimates the reduction in fusion yield, though the surface brightness profiles shapes (Figure 7) are qualitatively correct. Though the reduction of ion viscosity in DUED has a significant impact on fusion emissivity profile shapes (Figure 8), it has only a modest impact on the fusion yields. For vfl = 1 in DUED, $YOS_{DD} = 0.06$ and $YOS_{D3He} = 0.05$; for vfl = 0.25 in DUED, $YOS_{DD} = 0.07$ and $YOS_{D3He} = 0.06$. Similarly, other observables beyond the burn profile are not strongly affected by the reduction of ion viscosity in DUED, from $T_{i,DD} = 31.1\,\text{keV}$, $T_{i,D3He} = 33.4\,\text{keV}$, $R_{50,DD} = 62\,\mu\text{m}$, $R_{50,D3He} = 60\,\mu\text{m}$ with vfl = 1, to $T_{i,DD} = 29.1\,\text{keV}$, $T_{i,D3He} = 31.1\,\text{keV}$, $R_{50,DD} = 49\,\mu\text{m}$, $R_{50,D3He} = 48\,\mu\text{m}$ with vfl = 0.25. (In LASNEX, the reduction of vfl from 1 to 0.25 has a somewhat greater effect, increasing yields by of order $\sim 50\%$ while increasing the ion temperature by $\sim 10\%$ and decreasing the burn radius by $\sim 10\%$.) Thus, while the crude treatment of ion mean free path effects through the inclusion of ion diffusion in LASNEX and the reduction of ion viscosity in DUED more accurately capture fusion burn profile shapes and qualitatively represent some of the ion transport processes occurring in these implosions, quantitative discrepancies (e.g., in the yields) show that further theoretical refinement is needed to accurately treat these effects. This is a particularly salient illustration of the value of one-dimensional profile information, which shows significant variation based on different ion viscosity modeling in DUED in a way that the zero-dimensional integrated yield does not reflect.

Notably, the burn profile and yield data indicate that ion diffusion affects DD reactions more strongly than D^3He reactions, suggesting that deuterium ions are diffusing outward relative to ^3He ions toward the cooler regions of the fuel and also across the fuel-shell interface more rapidly than ^3He ions. This makes sense, given that deuterium has a mean free path a factor of 3.3 longer than ^3He, and it could be an indication of species separation effects.[19] Knudsen layer effects, which would impact D ions more strongly than ^3He ions, may also be responsible. The difference in behavior between DD and D^3He burn profile results is especially evident in the data at $3.1\,\text{mg/cm}^3$, where ion diffusion appears to affect the DD profile (Figure 7(b)) more strongly than the D^3He profile (Figure 7(d)). In comparison to the hydrodynamics-only simulation, the relative magnitude of the DD and D^3He profiles in the LASNEX simulation including diffusion is in better agreement with the relative magnitudes of the DD and D^3He profiles in the experimental data. The yield data indicate directly how ion diffusion brings the YOS_{DD} and YOS_{D3He} with respect to LASNEX into better agreement with each other, from $YOS_{DD} = 0.54$ and $YOS_{D3He} = 0.93$ to $YOS_{DD} = 0.82$ and $YOS_{D3He} = 0.83$. Thus, ion diffusion is able to eliminate the disparity between YOS_{DD} and YOS_{D3He} in hydro-only LASNEX. This result suggests that diffusion-related ion species separation is affecting the high-density experiments, as has been observed in separate but similar experiments,[19] and is likely affecting the low-density experiments as well.

In general, the use of burn profile measurements is critical in constraining modeling uncertainties and resolving discrepancies between different simulations. Additionally, these results motivate further development of kinetic-based models that can be compared to detailed data such as these spatially resolved fusion emission measurements. In addition to probing strongly kinetic-like conditions, it would also be interesting to compare simulated burn profiles to measurements of implosions at extremely low Knudsen number, such as was achieved in an indirectly-driven exploding pusher implosion at the NIF.[23] This implosion at $N_K \sim 0.01$, whose yield results ($\text{YOC} \sim 1$) are shown in Figure 1, produced extremely good agreement with the hydro-simulated yield, ion temperature, and other integrated quantities. It may be expected that hydrodyamic simulations could capture to very high accuracy the one-dimensional profile of fusion emission in this strongly hydrodynamic-like implosion.

In future experiments, an important complementary measurement that will be obtained is the profile of x-ray emission in the hot fuel region. Previous studies have shown correlations between the x-ray and nuclear emission profiles and spatial extent,[29] and such x-ray measurements may corroborate the interpretation of the nuclear data. In the present experiments, x-ray emission predominantly from the cooler shell region was imaged, so a direct comparison cannot be made.

Future directions for the investigation of ion kinetic effects in shock-driven implosions will include the development of a streaked PCIS system for time-resolved measurements of fusion burn profiles. Such data will be critical in constraining implosion models in a more detailed manner than with the existing time-integrated measurements. In particular, it may be possible to extract time-dependent, spatially resolved information about ion density and ion temperature, to observe how kinetic ion transport effects such as ion diffusion or Knudsen layer tail ion depletion alter the profiles of those quantities over the duration of the reaction history. As the ratio of DD to D^3He reactions is a strong function of the ion center-of-mass (CM) energy (or ion temperature in a Maxwellian plasma),[46] if the relative concentration of D and ^3He ions is known, the ratio of DD-p to D^3He-p emissivity may be used to infer profiles of ion CM energy. The use of time-integrated reaction profile measurements described above is a first step in the application of the PCIS technique, inferring the cumulative impact of ion diffusion.

VI. CONCLUSIONS

In summary, spatially resolved measurements of fusion reactions have been used to explore the impact of kinetic ion transport mechanisms, such as ion diffusion, in shock-driven ICF implosions where the ion mean free path approaches the size of the fuel region. Hydrodynamic models excluding ion diffusive effects have failed to capture the centrally peaked shape of measured DD and D^3He burn profiles for implosions where the Knudsen number is $N_K \sim 3$, while a model that incorporates classical ion diffusion produces burn profiles in better qualitative agreement with the measurements. A reduction of ion viscosity, a different modification of ion transport modeling, has a similar effect. In implosions characterized by shorter ion mean free paths and a Knudsen number of $N_K \sim 0.3$, ion diffusion has a smaller effect and purely hydrodynamic models reasonably match the experimental results. Thus, these results provide further evidence of the nature and magnitude of ion kinetic effects in greater detail than can be achieved through spatially integrated measurements such as the fusion yield. Quantitative discrepancies between measured and simulated yield results, in spite of the qualitative agreement between measured and simulated burn profile shapes, illustrate that further refinement of ion kinetic models is necessary to completely capture the experimental conditions. Additional future work aims to produce measurements that are simultaneously time-resolved and spatially resolved, so to observe the time evolution of fusion burn profiles and infer the real-time impact of ion kinetic effects.

ACKNOWLEDGMENTS

The authors thank R. Frankel and E. Doeg for contributing to the processing of CR-39 data used in this work, as well as the OMEGA operations crew for their help in executing these experiments. This work was performed in partial fulfillment of the first author's PhD thesis and supported in part by U.S. DoE (Grant Nos. DE-NA0001857, DE-FC52-08NA28752), FSC (No. 5-24431), NLUF (No. DE-NA0002035), LLE (No. 415935-G), LLNL (No. B597367). S. A. is supported by Italian grants PRIN 2012AY5LEL and Sapienza 2012 C26A12CZH2.

APPENDIX A: INFERRING BURN PROFILES FROM PENUMBRAL IMAGES

As discussed in Sec. II, the radial profile of nuclear burn is studied in spherical implosions. This approach and its application to OMEGA data have been described and used in Refs. 27 and 29 with slightly different terminology. The modeling described in those references was restricted to centrally-peaked burn profiles, since all of the data fell into that class, but since some of the simulations prepared for this work predicted hollow profiles the original family has been extended to include hollow burn profiles.[31]

The analysis is accomplished by forward fitting of the family of source profiles shown in Figure 3 and described in Sec. II, defined by the three parameters p ("peakedness," for shape), R_{50} (median burn radius, for size), and S_0 (a multiplier, for the yield). For reference, the mathematical forms of these profiles are described below by Eqs. (A1)–(A3). For computational simplicity used here is a different size parameter, r_0, but after the best-fit parameters are determined the more physical size parameter R_{50} is calculated from the result. The best fit to the data is found with a χ^2 analysis that also provides the parameter uncertainties.

$$\text{If } p > 0, \quad S(r) = S_0 e^{-\left(\frac{r}{r_0}\right)^{\frac{2}{p}}}, \tag{A1}$$

$$\text{If } p = 0, \quad S(r) = \begin{cases} 0, & \text{for } r > r_0, \\ S_0, & \text{for } r \le r_0, \end{cases} \tag{A2}$$

$$\text{If } p < 0, \quad S(r) = \begin{cases} 0, & \text{for } r > r_0, \\ S_0\left[2 - ae^{-b\left(\frac{r}{r_0}\right)^2}\right]^c, & \text{for } r \le r_0, \end{cases} \tag{A3}$$

where $a = 1 - p$, $b = \ln(1 - p)$, and $c = 2$ for $-1 < p < 0$; and $a = 2$, $b = \ln(2)$, and $c = -2p$ for $< p < -1$.

The measured radial derivative of proton fluence in the PCIS images (shifted to the penumbral region and scaled by the PCIS magnification) and the best-fit emissivity profiles forward fit to the measured data are shown in Figure 9. For both DD-p and D^3He-p data at both 0.4 mg/cm^3 and 3.1 mg/cm^3, the forward-fit emissivity profiles reasonably match the experimental data to within measurement uncertainty, with a reduced χ^2 of 1.32, 1.13, 1.10, and 2.85 for the data in Figures 9(a)–9(d), respectively. These results illustrate that the best fit profiles shown in Figure 5 are an appropriate inference of the experimental spatial burn profiles.

APPENDIX B: BURN PROFILE RESULTS IN COMPARISON TO OTHER SIMULATIONS

The comparison of fusion burn profile results from additional simulations to the measured burn profiles further demonstrates the value of these data in constraining various simulations and interpreting experimental results.

HYADES-simulated profiles of DD and D^3He reactions, though they exhibit significant qualitative differences relative to the previously shown LASNEX and DUED picture, roughly corroborate the discrepancies of burn profile shape relative to the data at lower initial gas densities. The simulated profiles at 0.4 mg/cm^3 and 3.1 mg/cm^3 are shown in Figure 10. At 0.4 mg/cm^3, the profiles are fairly flat, in contrast to the measured profiles, which are centrally peaked. Thus, in HYADES (with artificial viscosity only), as well as LASNEX and DUED (with physical ion viscosity), the predicted profiles at low density are too strongly weighted to the outer regions of the fuel. These results likely indicate the impact in the experiment of ion diffusion or other kinetic effects, which inhibit reactions near the fuel-shell interface. At 3.1 mg/cm^3, the HYADES-simulated profiles are centrally peaked, in qualitative agreement with the measured results. Again, it is expected that at higher initial gas density, with $N_K \sim 0.3$, ion kinetic

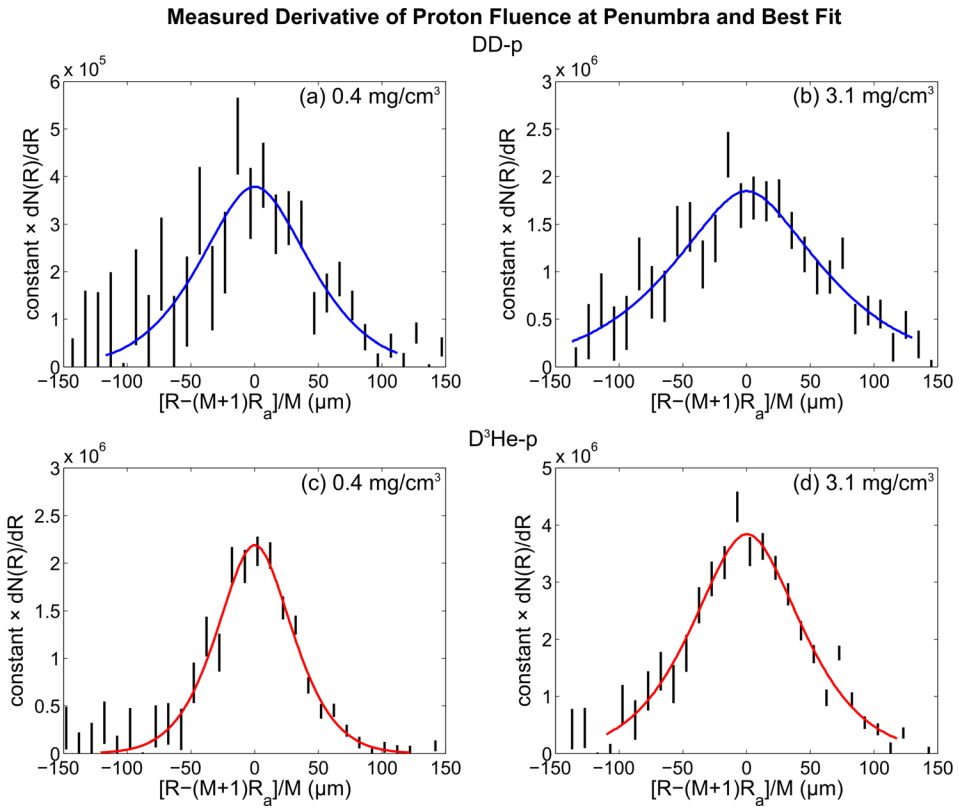

FIG. 9. Measured derivative of proton fluence (dN/dR, where N is the proton fluence and R is the radius in the proton fluence image) at the penumbra of the raw PCIS image, summed over the azimuthal angle, for (a)-(b) DD-p (blue) and (c)-(d) D^3He-p (red) in shock-driven implosions filled with (a),(c) 0.4 mg/cm^3 D^3He gas, in the kinetic regime, and (b), (d) 3.1 mg/cm^3 D^3He gas, in the hydrodynamic-like regime. The horizontal axis has been shifted and scaled to highlight the penumbral region, based the magnification M (the ratio of aperture-to-detector distance to implosion-to-aperture distance) and the aperture radius R_a. The vertical axis is scaled by the same constant factor in each plot, related to the magnification factor. The vertical black lines represent measurement uncertainty and the solid lines represent the best fit to those profiles. The uncertainty, mostly statistical, is larger at negative scaled radii (towards the center of the penumbral image), where the slope of the proton fluence is flatter.

effects are less significant and hydrodynamic models can more accurately capture the implosion dynamics and fusion production.

RIK-simulated surface brightness profiles of DD-p and D^3He-p emission for the implosion with 0.4 mg/cm^3 initial gas density, shown in Figure 11, confirm how ion kinetic processes are able to produce centrally peaked burn profiles. The profile shapes can be compared to measured and LASNEX-simulated surface brightness profiles in Figure 7. The RIK model, which includes ion diffusion and Knudsen-layer reduction of fusion reactivity, predicts centrally-peaked burn profiles in qualitative agreement with the LASNEX with ion diffusion model and also in qualitative agreement with the experimental results.

The measured burn profile sizes (R_{50}) and yields as a function of initial gas density are compared to the predictions of hydrodynamic and RIK simulations in Figure 12. These results show discrepancies between the hydrodynamic models and the data, which shed light on the inability of hydrodynamic models to capture key ion kinetic mechanisms that become important in the low-density experiments. While the measurements show a trend of increasing burn radius with increasing gas density, the HYADES simulations exhibit a maximum in predicted burn radius in the middle of the density range, falling off at both high density and low density. The DUED simulations (with ion viscosity, vfl = 1) show a flat trend. For both HYADES and DUED, the predicted R_{50} are smaller than the experimental values at high density, likely indicating a weaker convergence or a weaker ion temperature peak near the origin in the experiment than is predicted by the hydrodynamic codes. An unphysical temperature spike near the origin in hydrodynamic simulations will unduly weight the simulated reaction profile to smaller radii and skew the simulated R_{50} lower relative to what occurs in the experiments. At low initial gas density, the hydro-simulated ΔR_{50} differ significantly from what is observed experimentally. The experimental results show a larger burn region for DD reactions than for D^3He reactions,

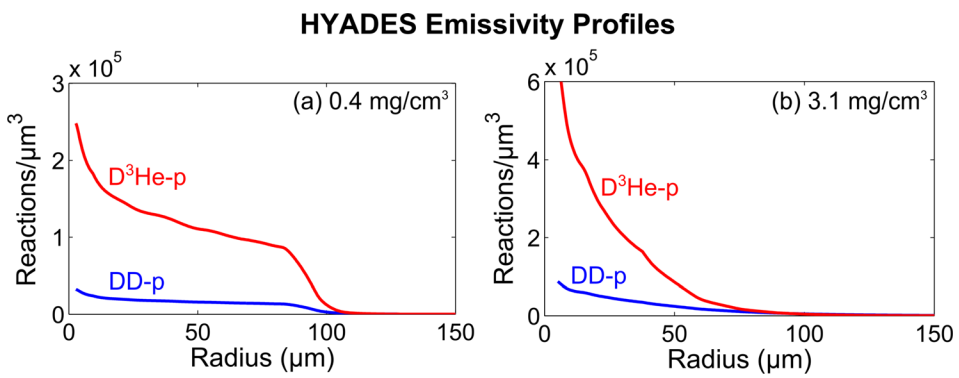

FIG. 10. HYADES-simulated profiles of DD and D^3He fusion emission, for implosions with initial gas densities of (a) 0.4 mg/cm^3 (left) and (b) 3.1 mg/cm^3 (right).

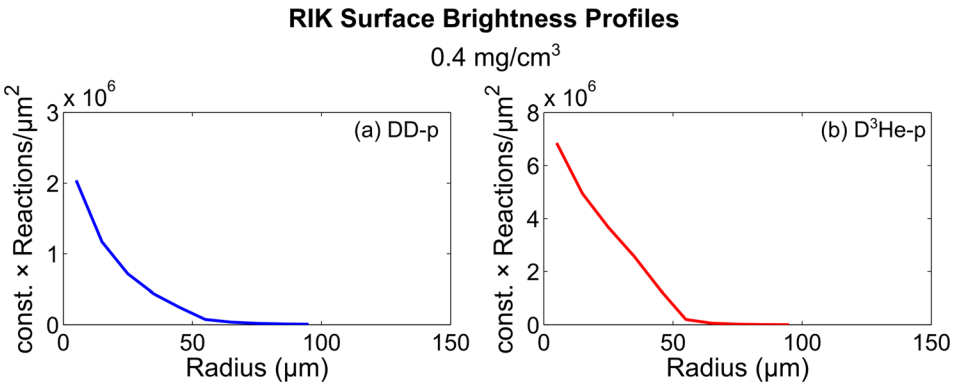

FIG. 11. Profiles of surface brightness of (a) DD-proton and (b) D^3He-proton emission in RIK simulations for the implosion with an initial gas density of 0.4 mg/cm^3. The profiles are scaled by a constant factor to match the total yield. At low initial gas density (long ion mean free path, $N_K \sim 3$), the RIK model, which includes ion diffusion and Knudsen-layer modification of the fusion reactivity, produces centrally peaked brightness profiles.

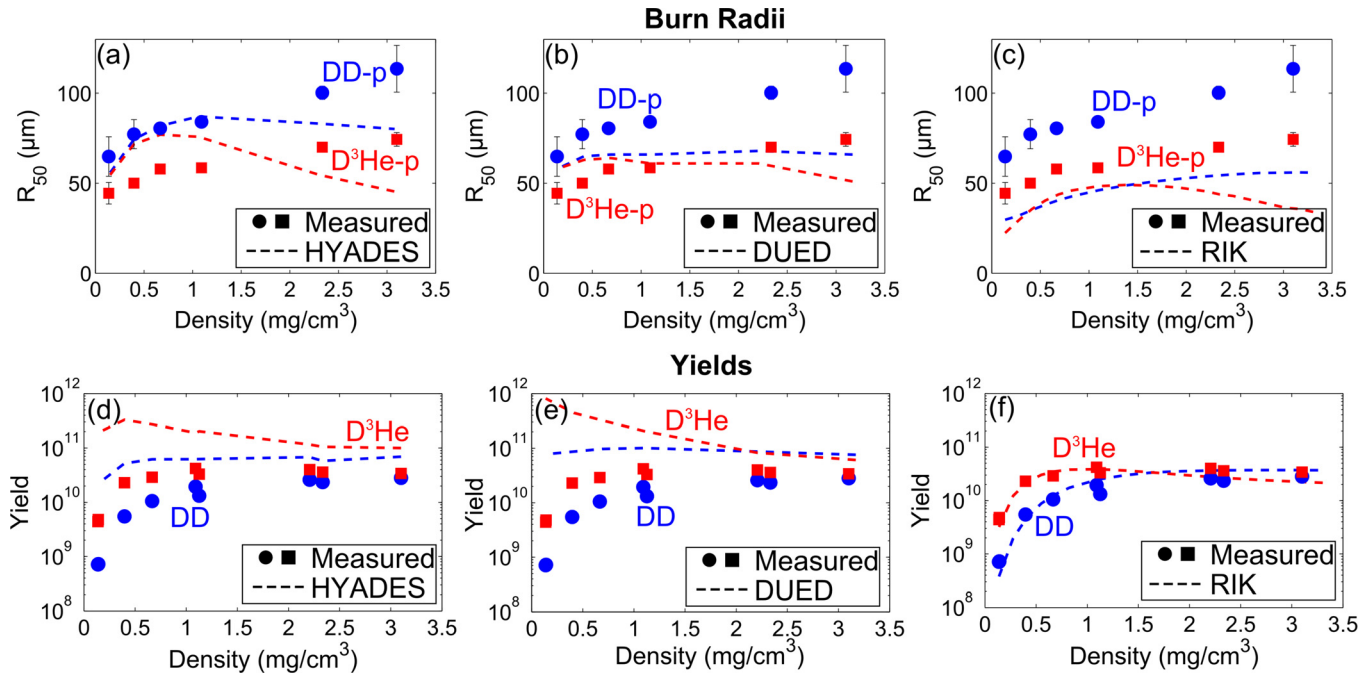

FIG. 12. Measured DD-p (blue circles) and D^3He-p (red squares) burn radii (characterized in terms of R_{50}) and yields as a function of initial gas density in comparison to (a),(d) HYADES hydrodynamics simulations (dashed lines), (b), (e) DUED hydrodynamics simulations (dashed lines), and (c), (f) reduced-ion-kinetic (RIK) simulations (dashed lines). (e) and (f) were originally presented in Ref. 6 and are reproduced with permission from Phys. Rev. Lett. **112**, 185001 (2014).

while HYADES and DUED predict a negligible ΔR_{50}. This discrepancy is likely the result of ion diffusion or similar long-mean-free-path mechanisms, which allow for D ions to reach larger radii than ^{3}He ions. This effect does not appear to be captured in the RIK model, which accounts for ion diffusion and Knudsen layer reduction of fusion reactivity, and shows only a modest ΔR_{50} at low density. The value of the burn radii at low initial gas density in HYADES and DUED appears to be in good overall agreement with the experimental values, though in both cases there is a factor of 10–100 difference between the measured and simulated yields. In contrast, the RIK model predicts quite accurately the total DD and D^3He yields, but appears to underestimate by almost a factor of 2 the magnitude of the burn radii. This discrepancy is likely the consequence of the predicted escape of fuel ions, which allows for a greatly reduced fuel density and increased shell convergence. For DD reactions, RIK approximately captures the monotonic trend of increasing R_{50} with increasing initial gas density. Additionally, as mentioned earlier, the LASNEX with ion diffusion simulations predict $R_{50,DD} = 100\,\mu$m and $R_{50,D3He} = 80\,\mu$m at 0.4 mg/cm^3 and $R_{50,DD} = 83\,\mu$m and $R_{50,D3He} = 68\,\mu$m at 3.1 mg/cm^3. This trend of R_{50} with initial gas density is opposite to that in the data, and this discrepancy may reflect the diffusion model overestimating the transport of fuel ions, as evidenced also by this simulation overestimating the reduction in fusion yield, at 0.4 mg/cm^3. These simulations will continue to be explored, and burn profile measurements such as those presented here offer a powerful constraint on implosion modeling and provide guidance on improvement of kinetic models such as those included in the RIK simulations.

[1]J. Nuckolls, L. Wood, A. Thiessen, and G. Zimmerman, Nature **239**, 139 (1972).
[2]H. Brysk and P. Hammerling, Phys. Rev. Lett. **34**, 502 (1975).
[3]E. K. Storm, H. G. Ahlstrom, M. J. Boyle, D. E. Campbell, L. W. Coleman, S. S. Glaros, H. N. Kornblum, R. A. Lerche, D. R. MacQuigg, D. W. Phillion, F. Rainer, R. Rienecker, V. C. Rupert, V. W. Silvinsky, D. Speck, C. Swift, and K. Tirsell, Phys. Rev. Lett. **40**, 1570 (1978).

[4]M. D. Rosen and J. H. Nuckolls, Phys. Fluids **22**, 1393 (1979).
[5]B. Ahlborn and M. H. Key, Plasma Phys. **23**, 435 (1981).
[6]M. J. Rosenberg, H. G. Rinderknecht, N. M. Hoffman, P. A. Amendt, S. Atzeni, A. B. Zylstra, C. K. Li, F. H. Séguin, H. Sio, M. G. Johnson, J. A. Frenje, R. D. Petrasso, V. Y. Glebov, C. Stoeckl, W. Seka, F. J. Marshall, J. A. Delettrez, T. C. Sangster, R. Betti, V. N. Goncharov, D. D. Meyerhofer, S. Skupsky, C. Bellei, J. Pino, S. C. Wilks, G. Kagan, K. Molvig, and A. Nikroo, Phys. Rev. Lett. **112**, 185001 (2014).
[7]H. G. Rinderknecht, H. Sio, C. K. Li, A. B. Zylstra, M. J. Rosenberg, P. Amendt, J. Delettrez, C. Bellei, J. A. Frenje, M. Gatu Johnson, F. H. Séguin, R. D. Petrasso, R. Betti, V. Y. Glebov, D. D. Meyerhofer, T. C. Sangster, C. Stoeckl, O. Landen, V. A. Smalyuk, S. Wilks, A. Greenwood, and A. Nikroo, Phys. Rev. Lett. **112**, 135001 (2014).
[8]J. R. Rygg, J. A. Frenje, C. K. Li, F. H. Séguin, R. D. Petrasso, J. A. Delettrez, V. Y. Glebov, V. N. Goncharov, D. D. Meyerhofer, S. P. Regan, and C. Stoeckl, Phys. Plasmas **13**, 052702 (2006).
[9]D. T. Casey, J. A. Frenje, M. G. Johnson, M. J.-E. Manuel, H. G. Rinderknecht, N. Sinenian, F. H. Séguin, C. K. Li, R. D. Petrasso, P. B. Radha, J. A. Delettrez, V. Y. Glebov, D. D. Meyerhofer, T. C. Sangster, D. P. McNabb, P. A. Amendt, R. N. Boyd, J. R. Rygg, H. W. Herrmann, Y. H. Kim, and A. D. Bacher, Phys. Rev. Lett. **108**, 075002 (2012).
[10]H. W. Herrmann, J. R. Langenbrunner, J. M. Mack, J. H. Cooley, D. C. Wilson, S. C. Evans, T. J. Sedillo, G. A. Kyrala, S. E. Caldwell, C. S. Young, A. Nobile, J. Wermer, S. Paglieri, A. M. McEvoy, Y. Kim, S. H. Batha, C. J. Horsfield, D. Drew, W. Garbett, M. Rubery, V. Y. Glebov, S. Roberts, and J. A. Frenje, Phys. Plasmas **16**, 056312 (2009).
[11]P. Amendt, O. L. Landen, H. F. Robey, C. K. Li, and R. D. Petrasso, Phys. Rev. Lett. **105**, 115005 (2010).
[12]G. Kagan and X.-Z. Tang, Phys. Plasmas **19**, 082709 (2012).
[13]C. Bellei, P. A. Amendt, S. C. Wilks, M. G. Haines, D. T. Casey, C. K. Li, R. Petrasso, and D. R. Welch, Phys. Plasmas **20**, 012701 (2013).
[14]G. Kagan and X.-Z. Tang, Phys. Lett. A **378**, 1531 (2014).
[15]D. B. Henderson, Phys. Rev. Lett. **33**, 1142 (1974).
[16]K. Molvig, N. M. Hoffman, B. J. Albright, E. M. Nelson, and R. B. Webster, Phys. Rev. Lett. **109**, 095001 (2012).
[17]O. Larroche, Eur. Phys. J. D **27**, 131 (2003).
[18]O. Larroche, Phys. Plasmas **19**, 122706 (2012).
[19]H. G. Rinderknecht, M. J. Rosenberg, C. K. Li, N. M. Hoffman, G. Kagan, A. B. Zylstra, H. Sio, J. A. Frenje, M. Gatu Johnson, F. H. Séguin, R. D. Petrasso, P. Amendt, C. Bellei, S. Wilks, J. Delettrez, V. Y. Glebov, C. Stoeckl, T. C. Sangster, D. D. Meyerhofer, and A. Nikroo, Phys. Rev. Lett. **114**, 025001 (2015).
[20]T. R. Boehly, D. L. Brown, R. S. Craxton, R. L. Keck, J. P. Knauer, J. H. Kelly, T. J. Kessler, S. A. Kumpan, S. J. Loucks, S. A. Letzring, F. J. Marshall, R. L. McCrory, S. F. B. Morse, W. Seka, J. M. Soures, and C. P. Verdon, Opt. Commun. **133**, 495 (1997).
[21]G. Miller, E. Moses, and C. Wuest, Opt. Eng. **43**, 2841 (2004).
[22]M. J. Rosenberg, A. B. Zylstra, F. H. Séguin, H. G. Rinderknecht, J. A. Frenje, M. Gatu Johnson, H. Sio, C. J. Waugh, N. Sinenian, C. K. Li, R. D. Petrasso, P. W. McKenty, M. Hohenberger, P. B. Radha, J. A. Delettrez, V. Y. Glebov, R. Betti, V. N. Goncharov, J. P. Knauer, T. C. Sangster, S. LePape, A. J. Mackinnon, J. Pino, J. M. McNaney, J. R. Rygg, P. A. Amendt, C. Bellei, L. R. Benedetti, L. Berzak Hopkins, R. M. Bionta, D. T. Casey, L. Divol, M. J. Edwards, S. Glenn, S. H. Glenzer, D. G. Hicks, J. R. Kimbrough, O. L. Landen, J. D. Lindl, T. Ma, A. MacPhee, N. B. Meezan, J. D. Moody, M. J. Moran, H.-S. Park, B. A. Remington, H. Robey, M. D. Rosen, S. C. Wilks, R. A. Zacharias, H. W. Herrmann, N. M. Hoffman, G. A. Kyrala, R. J. Leeper, R. E. Olson, J. D. Kilkenny, and A. Nikroo, Phys. Plasmas **21**, 122712 (2014).
[23]S. Le Pape, L. Divol, L. Berzak Hopkins, A. Mackinnon, N. B. Meezan, D. Casey, J. Frenje, H. Herrmann, J. McNaney, T. Ma, K. Widmann, A. Pak, G. Grimm, J. Knauer, R. Petrasso, A. Zylstra, H. Rinderknecht, M. Rosenberg, M. Gatu-Johnson, and J. D. Kilkenny, Phys. Rev. Lett. **112**, 225002 (2014).
[24]S. Skupsky, J. A. Marozas, R. S. Craxton, R. Betti, T. J. B. Collins, J. A. Delettrez, V. N. Goncharov, P. W. McKenty, P. B. Radha, T. R. Boehly, J. P. Knauer, F. J. Marshall, D. R. Harding, J. D. Kilkenny, D. D. Meyerhofer, T. C. Sangster, and R. L. McCrory, Phys. Plasmas **11**, 2763 (2004).
[25]O. Hurricane, D. Callahan, D. Casey, P. Celliers, C. Cerjan, E. Dewald, T. Dittrich, T. Döppner, D. Hinkel, L. B. Hopkins, J. Kline, S. LePape, T. Ma, A. MacPhee, J. Milovich, A. Pak, H.-S. Park, P. Patel, B. Remington, J. Salmonson, P. Springer, and R. Tommasini, Nature **506**, 343 (2014).
[26]T. C. Sangster, V. N. Goncharov, R. Betti, P. B. Radha, T. R. Boehly, D. T. Casey, T. J. B. Collins, R. S. Craxton, J. A. Delettrez, D. H. Edgell, R. Epstein, C. J. Forrest, J. A. Frenje, D. H. Froula, M. Gatu-Johnson, Y. Y. Glebov, D. R. Harding, M. Hohenberger, S. X. Hu, I. V. Igumenshchev, R. Janezic, J. H. Kelly, T. J. Kessler, C. Kingsley, T. Z. Kosc, J. P. Knauer, S. J. Loucks, J. A. Marozas, F. J. Marshall, A. V. Maximov, R. L. McCrory, P. W. McKenty, D. D. Meyerhofer, D. T. Michel, J. F. Myatt, R. D. Petrasso, S. P. Regan, W. Seka, W. T. Shmayda, R. W. Short, A. Shvydky, S. Skupsky, J. M. Soures, C. Stoeckl, W. Theobald, V. Versteeg, B. Yaakobi, and J. D. Zuegel, Phys. Plasmas **20**, 056317 (2013).
[27]F. H. Séguin, J. L. Deciantis, J. A. Frenje, S. Kurebayashi, C. K. Li, C. Chen, V. Berube, B. E. Schwartz, R. D. Petrasso, V. A. Smalyuk, F. J. Marshall, J. P. Knauer, J. A. Delettrez, P. W. McKenty, D. D. Meyerhofer, S. Roberts, T. C. Sangster, K. Mikaelian, and H. S. Park, Rev. Sci. Instrum. **75**, 3520 (2004).
[28]J. L. DeCiantis, F. H. Séguin, J. A. Frenje, V. Berube, M. J. Canavan, C. D. Chen, S. Kurebayashi, C. K. Li, J. R. Rygg, B. E. Schwartz, R. D. Petrasso, J. A. Delettrez, S. P. Regan, V. A. Smalyuk, J. P. Knauer, F. J. Marshall, D. D. Meyerhofer, S. Roberts, T. C. Sangster, C. Stoeckl, K. Mikaelian, H. S. Park, and H. F. Robey, Rev. Sci. Instrum. **77**, 043503 (2006).
[29]F. H. Séguin, J. L. DeCiantis, J. A. Frenje, C. K. Li, J. R. Rygg, C. D. Chen, R. D. Petrasso, J. A. Delettrez, S. P. Regan, V. A. Smalyuk, V. Y. Glebov, J. P. Knauer, F. J. Marshall, D. D. Meyerhofer, S. Roberts, T. C. Sangster, C. Stoeckl, K. Mikaelian, H. S. Park, H. F. Robey, and R. E. Tipton, Phys. Plasmas **13**, 082704 (2006).
[30]On some experiments, a second PCIS at a different position was fielded with only a single piece of CR-39, filtered by 1100 μm Al, to detect D^3He protons.
[31]F. H. Séguin, H. G. Rinderknecht, M. Rosenberg, A. Zylstra, J. Frenje, C. K. Li, R. Petrasso, F. J. Marshall, T. C. Sangster, N. M. Hoffman, P. A. Amendt, C. B. ad, S. Le Pape, and S. C. Wilks, Bull. Am. Phys. Soc. **59**, 15 (2014).
[32]S. Atzeni, Comput. Phys. Commun. **43**, 107 (1986).
[33]S. Atzeni, A. Schiavi, F. Califano, F. Cattani, F. Cornolti, D. Del Sarto, T. Liseykina, A. Macchi, and F. Pegoraro, Comput. Phys. Commun. **169**, 153 (2005).
[34]W. Seka, H. A. Baldis, J. Fuchs, S. P. Regan, D. D. Meyerhofer, C. Stoeckl, B. Yaakobi, R. S. Craxton, and R. W. Short, Phys. Rev. Lett. **89**, 175002 (2002).
[35]C. Stoeckl, V. Y. Glebov, S. Roberts, T. C. Sangster, R. A. Lerche, R. L. Griffith, and C. Sorce, Rev. Sci. Instrum. **74**, 1713 (2003).
[36]G. B. Zimmerman and W. L. Kreur, Comments Plasma Phys. Controlled Fusion **2**, 51 (1975).
[37]R. W. Schunk, Rev. Geophys. **15**, 429, doi:10.1029/RG015i004p00429 (1977).
[38]J. T. Larsen and S. M. Lane, J. Quant. Spectrosc. Radiat. Transfer **51**, 179 (1994).
[39]N. M. Hoffman, G. B. Zimmerman, K. Molvig, H. G. Rinderknecht, M. J. Rosenberg, B. J. Albright, A. N. Simakov, H. Sio, A. B. Zylstra, M. G. Johnson, F. H. Séguin, J. A. Frenje, C. K. Li, R. D. Petrasso, D. M. Higdon, G. Srinivasan, V. Yu. Glebov, C. Stoeckl, W. Seka, and T. Craig Sangster, Phys. Plasmas **22**, 052707 (2015).
[40]B. J. Albright, K. Molvig, C.-K. Huang, A. N. Simakov, E. S. Dodd, N. M. Hoffman, G. Kagan, and P. F. Schmit, Phys. Plasmas **20**, 122705 (2013).
[41]N. Hoffman *et al.*, Bull. Am. Phys. Soc. **58**, 16 (2013).
[42]W. D. Schulz, in *Methods in Computational Physics*, edited by B. Alder, S. Fernbach, and M. Rotenberg (Academic Press, New York, 1964), Vol. 3, p. 1.
[43]V. Y. Glebov, C. Stoeckl, T. C. Sangster, S. Roberts, G. J. Schmid, R. A. Lerche, and M. J. Moran, Rev. Sci. Instrum. **75**, 3559 (2004).
[44]F. H. Séguin, J. A. Frenje, C. K. Li, D. G. Hicks, S. Kurebayashi, J. R. Rygg, B.-E. Schwartz, R. D. Petrasso, S. Roberts, J. M. Soures, D. D. Meyerhofer, T. C. Sangster, J. P. Knauer, C. Sorce, V. Y. Glebov, C. Stoeckl, T. W. Phillips, R. J. Leeper, K. Fletcher, and S. Padalino, Rev. Sci. Instrum. **74**, 975 (2003).
[45]At 3.1 mg/cm^3, a DD yield of 1.4×10^{10} and a D^3He yield of 2.5×10^{10} are inferred from PCIS. At 0.4 mg/cm^3, a DD yield of 2.5×10^9 and a D^3He yield of 1.0×10^{10} are inferred from PCIS.
[46]C. K. Li, D. G. Hicks, F. H. Séguin, J. A. Frenje, R. D. Petrasso, J. M. Soures, P. B. Radha, V. Y. Glebov, C. Stoeckl, D. R. Harding, J. P. Knauer, R. Kremens, F. J. Marshall, D. D. Meyerhofer, S. Skupsky, S. Roberts, C. Sorce, T. C. Sangster, T. W. Phillips, M. D. Cable, and R. J. Leeper, Phys. Plasmas **7**, 2578 (2000).